Synthesis, characterisation, and crystal structure of a novel U(V) brannerite UTi1.23Al0.77O6 and the UTi2-xAlxO6 system

Dixon Wilkins, M. C.; Mottram, L. M.; Maddrell, E. R.; Stennett, M. C.; Corkhill, C. L.; Kvashnina, K. O.; Hyatt, N. C.;

Originally published:

November 2021

Inorganic Chemistry 60(2021)23, 18112-18121

DOI: https://doi.org/10.1021/acs.inorgchem.1c02733

Synthesis, characterisation, and crystal structure of a novel U(V) brannerite $UTi_{1.23}Al_{0.77}O_6$ and the $UTi_{2-x}Al_xO_6$ system

Malin C. Dixon Wilkins[1], Lucy M. Mottram[1], Ewan R. Maddrell[2], Martin C. Stennett[1], Claire L. Corkhill,[1], Kristina O. Kvashnina,[3,4] and Neil C. Hyatt[1]*

[1]Department of Materials Science and Engineering, University of Sheffield, Sheffield, UK

[2]National Nuclear Laboratory, Sellafield, Cumbria, UK

[3]The Rossendorf Beamline at ESRF, CS 40220, 38043 Grenoble Cedex 9, France

[4]Helmholtz-Zentrum Dresden-Rossendorf, Institute of Resource Ecology, Bautzner Landstrasse 400, 01328 Dresden, Germany

*Corresponding author: n.c.hyatt@sheffield.ac.uk

Abstract

The synthesis, characterisation and crystal structure of a novel U^{5+} (dominant) brannerite of composition $U_{1.09(6)}Ti_{1.29(3)}Al_{0.71(3)}O_6$ is reported, as determined from Rietveld analysis of high resolution powder neutron diffraction data. Examination of the $UTi_{2-x}Al_xO_6$ system demonstrated the formation of brannerite structured compounds with varying Al^{3+} and U^{5+} content, from $U_{0.93(6)}Ti_{1.64(3)}Al_{0.36(3)}O_6$ to $U_{0.89(6)}Ti_{1.00(3)}Al_{1.00(3)}O_6$. Substitution of $Al^{3+}$for Ti^{4+}, with U^{5+} charge compensation, resulted in near-linear changes in the *b* and *c* unit cell parameters and the overall unit cell volume, as expected from ionic radii considerations. The presence of U^{5+} as the dominant oxidation state in near single phase brannerite compositions was evidenced by complementary laboratory U L_3 edge and high energy resolution fluorescence detected (HERFD) U M_4 edge X-ray Absorption Near Edge Spectroscopy. No brannerite phase was found for compositions with Al^{3+} / $Ti^{4+} > 1$, which would require U^{6+} contribution for charge compensation. These data expand the crystal chemistry of uranium brannerites to the stabilisation of dominant U^{5+} brannerites by substitution of trivalent cations, such as Al^{3+}, on the Ti^{4+} site.

1. Introduction

Synthetic analogues of thermodynamically stable titanate mineral phases have been considered for their suitability as durable ceramic wasteforms for high actinide content nuclear wastes. One of the more promising minerals is brannerite (prototypically UTi_2O_6), with natural samples displaying the ability to retain a large fraction of their initial U content despite high degrees of metamictisation and alteration.[1–3] Though the radiation tolerance[4,5] and aqueous durability[6,7] of brannerites are not as high as some other materials (with critical amorphisation doses of 0.8 to 1.5 × 10^{14} ions cm^{-2}, compared with 2 to 6 × 10^{14} ions cm^{-2} for synthetic zirconolites and pyrochlores), UTi_2O_6 remains a particularly attractive host for actinides because of its notably high U content (55.4% U by weight), and so high waste loading.

It has been established that the synthesis of UTi_2O_6 requires heat treatment(s) under a low pO_2 atmosphere in order to retain U^{4+}.[8–11] The substitution of U^{4+} by a lower valent dopant has also been widely applied in the synthesis of U^{5+} brannerites in air atmospheres.[8,12–14] It should be noted that much of the recent work on brannerites has examined the formation of a brannerite ceramic phase within a glass-ceramic composite (commonly within the $Na_2AlBSi_6O_{16}$ glass system), though in most cases the impact of the glass phase on the brannerite phase crystal chemistry is limited (*i.e.* it is expected that the synthesis of a pure ceramic brannerite of the same composition would be facile).[11,15–19]

Common U-site charge-balancing dopants include Ca^{2+}, Y^{3+}, and trivalent lanthanides (notably Ce^{3+} and Gd^{3+}), resulting in U^{5+} brannerites (*e.g.* $U^{5+}_{0.5}Y^{3+}_{0.5}Ti_2O_6$).[8,13,15–17,20] In addition to materials specifically targeting U^{5+}, other doped or mixed U-site brannerites have been reported, including: $(U_{0.9}Ce_{0.1})_{1-x}Gd_xTi_2O_6$, where Ce was utilised as an analogue of Pu[21,22]; $U_{1-x}Ce_xTi_2O_6$,

with average Ce oxidation states varying significantly according to process conditions[15,19]; and $Gd_{0.2}Hf_{0.2}U_{0.4}Pu_{0.2}Ti_2O_6$.[17]

In contrast to the significant volume of work on U-site doped brannerites, little attention has been directed to the possibility of charge-balancing U^{5+} *via* dopants on the Ti-site. Materials with stoichiometries of $UTi_{1.8}Fe_{0.2}O_6$ and $UTi_{1.6}Fe_{0.4}O_6$ were reported to form near single phase brannerites when synthesised under Ar, but formed a mixture of brannerite-structured $UTi_{1.60}Fe_{0.49}O_6$, and the binary oxides U_3O_8 and TiO_2 when synthesis was attempted in air.[8,23,24] In the same work, the paired self-charge compensated substitution of Gd+Nb for U+Ti (overall $U_{1-x}Gd_xTi_{2-x}Nb_xO_6$) was examined, with materials synthesised under Ar. For x = 0.1 and 0.2, near single phase brannerites of the nominal compositions were produced, with the material batched with x = 0.5 forming a multiphase mixture containing brannerite phase $Gd_{0.67}U_{0.29}Ti_{1.29}Nb_{0.72}O_6$.

A previous report of the ion size limits in the brannerite structure found that the Ti-site of Th brannerite ($ThTi_2O_6$, thorutite) could not be significantly expanded (by doping with Sn^{4+} or Zr^{4+}) or contracted (by doping with Ge^{4+}).[25] In this work, materials across the compositional system $UTi_{2-x}Al_xO_6$ have been synthesised in air and characterised to identify the solubility and impact of a high fraction, lower valence Ti-site dopant on the formation of, and U oxidation state in, U brannerite. The use of Ti-site dopants to stabilise U^{5+} brannerites is notable in that, compared to U-site doping, the high U content is retained, where otherwise up to 0.5 f.u. would be substituted for the charge-balancing element.

2. Experimental

Samples were prepared by a standard cold-press and sinter solid state route. Stoichiometric amounts of UO_2 (ABSCO limited), TiO_2 (rutile, Sigma Aldrich), and Al_2O_3 (Sigma Aldrich) were

homogenised by planetary milling (500 rpm, 10 minutes, Retsch PM100) utilising yttria-stabilised zirconia mill pots and milling media, with isopropanol as a carrier fluid. The milled slurries were dried at 85 °C, and the resulting powder cakes broken up by hand in a mortar and pestle. The milled powders were then pressed into 10 mm pellets under 2 t (approx. 250 MPa). Pellets were heat treated in alumina crucibles at 1400 °C for 48 hours in air.

X-ray diffraction (XRD) patterns of each sample were collected on powdered material (Bruker D2 Phaser, Ni-filtered Cu K_α radiation). Phase analysis was conducted by matching the reflections observed to phases in the PDF-4+ database.[26] Unit cell parameters of each brannerite phase were derived using LeBail method refinements, utilising the Topas[27] and JEdit[28] software packages. The background of each diffraction pattern was modelled with an eight term shifted Chebyshev polynomial; peak shapes resulting from instrumental and sample-based contributions were modelled using a Pearson VII function. Additional phases including Al_2O_3, Al_2TiO_5, TiO_2-rutile, and U_3O_8 were added according to the phases identified in the diffraction patterns.

The time-of-flight neutron diffraction pattern of a near-single phase sample with nominal composition $UTiAlO_6$ was collected at the High Resolution Powder Diffraction beamline (HRPD) at the ISIS neutron and muon source, Rutherford Appleton Laboratory, UK.[29] Approximately 3.5 g of material was packed into a vanadium metal can which was then sealed with indium wire. Data was collected over three banks, with a data collection time of *ca.* 5 hours; data from the backscattering bank ($158.46° < 2\theta < 176.11°$; $\Delta d/d \sim 6\times10^{-4}$) was utilised for structure refinement. Data normalisation and reduction were performed in the Mantid open source software package.[30] Rietveld method refinements were used to examine the structure, utilising the Topas[27] and JEdit[28] software packages.

The semi-quantitative chemical composition of each brannerite phase was determined by scanning electron microscopy with coupled energy dispersive X-ray spectroscopy (SEM/EDX). Solid samples were prepared for SEM/EDX analysis by mounting in a cold-set epoxy resin, polishing with increasingly fine grades of diamond suspensions, before coating with a conductive carbon layer. Due to the semi-quantitative nature of the EDX measurements and low accuracy of oxygen determination, a stoichiometric oxygen content was assumed.

U L_3 edge XANES were collected using a modified EasyXAFS XES100 extended spectrometer, utilising a 100 W Pd-anode X-ray tube and operating in Rowland circle geometry.[31,32] Samples were prepared by pressing pellets of sufficient material to form one absorption length mixed with a polyethylene glycol binder (approximately 45 mg). Data were acquired by placing samples in front of a Hitatchi Vortex Silicon Drift Detector (SDD), with a 5 mm exit slit to minimise stray scatter. The energy resolution of the SDD is ca. 140 eV, enabling rejection of the harmonic content of the incident beam and background scatter. X-ray energies were selected using the (1266) harmonic of a Si (211) spherically bent crystal analyser. A He flight path (welded steel enclosure with kapton windows) was employed to minimise air scatter and absorption. Data were acquired with ($I_t(E)$) and without the sample ($I_0(E)$), using the same scan parameters. A step size of 0.5 eV and count time of 20s / step were used in the XANES region, in the pre- and post-edge regions the step size was 1.0 eV with a count time of 10s / step. Typically, 10 spectra were acquired for each composition and summed, the total data collection time was around 20 h for each composition. The absolute energy scale was calibrated using a reference of Y_2O_3 (E_0 = 17042.30 eV), with E_0 set as first peak in first derivative (the Y_2O_3 reference was previously calibrated against Y-foil[33]). Spectra were corrected to the absolute energy scale and for leakage effects, as described by Mottram *et*

al.,[33] and further processed in Athena, part of the Demeter software package.[34,35] Spectra of well-characterised specimens of UTi_2O_6, $U_{0.5}Yb_{0.5}Ti_2O_6$, and $CaUO_4$ were also collected to act as reference compounds of known U valence (U^{4+}, U^{5+}, and U^{6+} respectively).

High Energy Resolution Fluorescence Detected (HERFD) U M_4 edge XANES were collected at ESRF beamlineBM20 (Ref. Scheinost (1)). The incident energy was selected using the <111> reflection from a double Si crystal monochromator. XANES spectra was measured in high-energy-resolution fluorescence detected (HERFD) mode using an X-ray emission spectrometer(2). The sample, analyzer crystal and photon detector (silicon drift detector) were arranged in a vertical Rowland geometry. The U HERFD spectra at the M_4 edge were obtained by recording the maximum intensity of the U Mb emission line (~3337 eV) as a function of the incident energy. The emission energy was selected using the <220> reflection of five spherically bent striped Si crystal analyzers (with 1m bending radius) aligned at 75° Bragg angle. The paths of the incident and emitted X-rays through air were minimized in order to avoid losses in intensity due to absorption.

1. Scheinost AC, Claussner J, Exner J, Feig M, Findeisen S, Hennig C, et al. ROBL-II at ESRF: a synchrotron toolbox for actinide research. J Synchrotron Radiat [Internet]. 2021 Jan 1;28(1):333–49. Available from: https://scripts.iucr.org/cgi-bin/paper?S1600577520014265

2. Kvashnina KO, Scheinost AC. A Johann-type X-ray emission spectrometer at the Rossendorf beamline. J Synchrotron Radiat. 2016;23:836–41.

Spectra were processed and linear combination fitting performed in Athena, part of the Demeter software package[34,35]. Spectra of well-characterised specimens of UTi_2O_6, $CrUO_4$, and $CaUO_4$ were also collected to act as reference compounds of known U valence (U^{4+}, U^{5+}, and U^{6+} respectively).

3. Results

3.1. X-ray diffraction

X-ray diffraction was used to determine the phases present in each composition, which are summarised in Table 1. A phase with the brannerite structure (UTi_2O_6; PDF #01-084-0496) was formed in all compositions examined except the end-members UTi_2O_6 and UAl_2O_6. The brannerite phase was the major crystalline phase identified in materials with nominal stoichiometries of $UTi_{2-x}Al_xO_6$ with $0.4 \leq x \leq 1.6$, inclusive. As the relative Al content increased, the brannerite unit cell volume decreased, as determined by LeBail refinements as discussed further below.

In the end-member composition UTi_2O_6 the only crystalline phases present were TiO_2 (rutile; PDF #01-070-7347) and U_3O_8 (PDF #04-006-7307), in agreement with literature reports of the attempted synthesis of UTi_2O_6 in air.[8] The nominal end-member composition UAl_2O_6 comprised only Al_2O_3 (corundum; PDF #04-006-3495) and U_3O_8.

At low Al incorporation, in nominal composition $UTi_{1.8}Al_{0.2}O_6$, a relatively small amount of brannerite phase was formed, and TiO_2 and U_3O_8 remained the major components. For nominal compositions in the range $UTi_{2-x}Al_xO_6$ $0.4 \leq x \leq 1.0$, U_3O_8 was no longer observed as an accessory phase. Compositions with $x > 1.0$ contained increasing amounts of U_3O_8, Al_2O_3 and Al_2TiO_5. TiO_2 (rutile) was observed in all samples with as-batched Ti / Al > 1, *i.e.* those with nominal compositions from UTi_2O_6 to $UTi_{1.2}Al_{0.8}O_6$; the relative amount of TiO_2 present decreased from a maximum in UTi_2O_6, to only a trace amount in $UTi_{1.2}Al_{0.8}O_6$.

Al_2O_3 and Al_2TiO_5 (PDF #00-041-0258) were observed as accessory phases. Al_2O_3 was observed in increasing amounts in all samples with nominal Al incorporation of $0.8 \leq x \leq 2.0$ (*i.e.* $UTi_{1.2}Al_{0.8}O_6$ to UAl_2O_6). Al_2TiO_5, with a pseudobrookite structure, was observed alongside Al_2O_3 in nominal compositions $UTi_{1.2}Al_{0.8}O_6$ and $UTi_{1.0}Al_{1.0}O_6$.

Table 1: Phases identified in the XRD patterns of materials with nominal compositions in the system $UTi_{2-x}Al_xO_6$ heat treated in air. The compositions of the brannerite phases present in each material as derived from semi-quantitative EDX measurements are also shown.

Nominal x in $UTi_{2-x}Al_xO_6$	Brannerite	U_3O_8	TiO_2	Al_2O_3	Al_2TiO_5	Brannerite composition (EDX)
0	-	Y	Y	-	-	N/A
0.2	Y	Y	Y	-	-	$U_{0.93(6)}Ti_{1.64(3)}Al_{0.36(3)}O_6$
0.4	Y	-	Y	-	-	$U_{1.04(6)}Ti_{1.53(3)}Al_{0.47(3)}O_6$
0.6	Y	-	Y	-	-	$U_{1.05(6)}Ti_{1.46(3)}Al_{0.54(3)}O_6$
0.8	Y	-	Y	Y	Y	$U_{1.06(6)}Ti_{1.40(3)}Al_{0.60(3)}O_6$
1.0	Y	-	-	Y	Y	$U_{1.09(6)}Ti_{1.29(3)}Al_{0.71(3)}O_6$
1.2	Y	Y	-	Y	-	$U_{1.00(6)}Ti_{1.27(3)}Al_{0.73(3)}O_6$
1.4	Y	Y	-	Y	-	$U_{0.98(6)}Ti_{1.22(3)}Al_{0.78(3)}O_6$
1.6	Y	Y	-	Y	-	$U_{0.91(6)}Ti_{1.01(3)}Al_{0.99(3)}O_6$
1.8	Y	Y	-	Y	-	$U_{0.89(6)}Ti_{1.00(3)}Al_{1.00(3)}O_6$
2.0	-	Y	-	Y	-	N/A

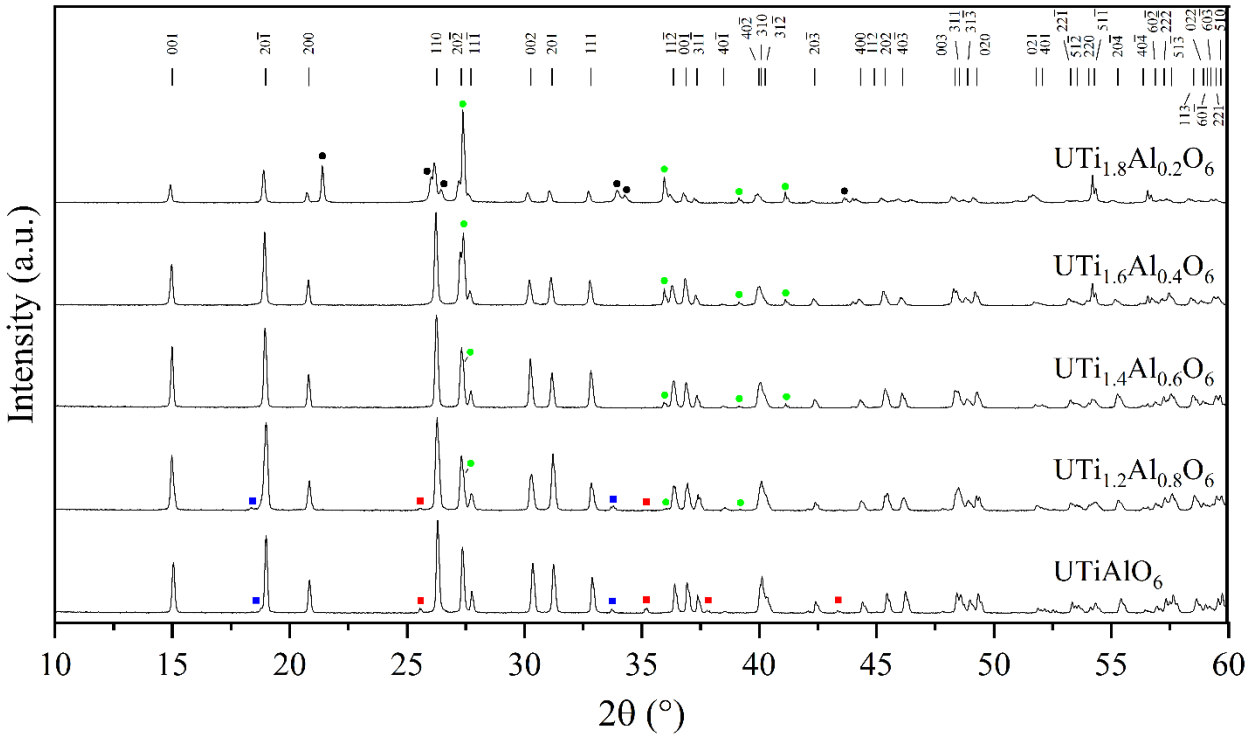

Figure 1: X-ray diffraction patterns of materials with nominal compositions in the system $UTi_{2-x}Al_xO_6$, where $0 \leq x \leq 1$. Only those compositions that formed brannerite are shown. Tick marks below display the

positions of reflections of a brannerite structure with unit cell parameters approximating those of $UTiAlO_6$. Reflections indexed to non-brannerite phases are marked with symbols: black circle, U_3O_8; green circle, TiO_2 (rutile); red square, Al_2O_3 (corundum); blue square, Al_2TiO_5.

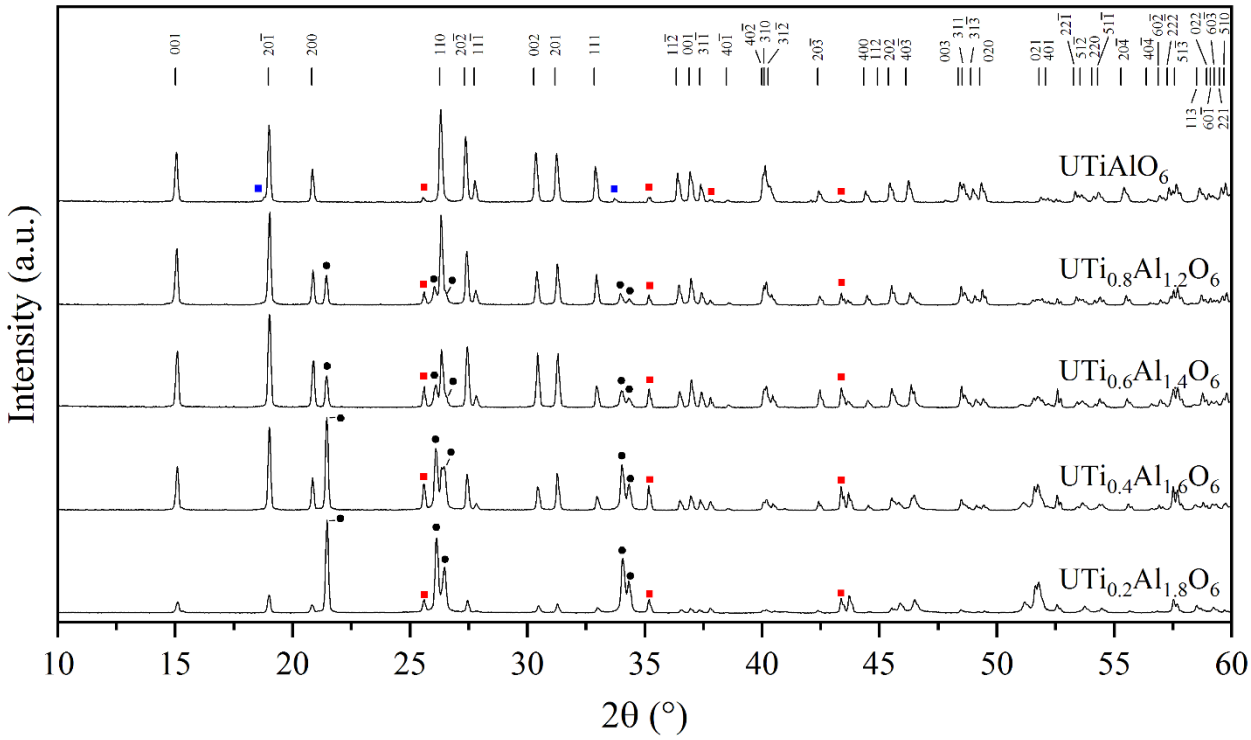

Figure 2: X-ray diffraction patterns of materials with nominal compositions in the system $UTi_{2-x}Al_xO_6$, where $1 \leq x \leq 2$. Only those compositions that formed brannerite are shown. Tick marks below display the positions of reflections of a brannerite structure with unit cell parameters approximating those of $UTiAlO_6$. Reflections indexed to non-brannerite phases are marked with symbols: black circle, U_3O_8; green circle, TiO_2 (rutile); red square, Al_2O_3 (corundum); blue square, Al_2TiO_5.

3.2. Neutron diffraction

Time of flight neutron diffraction data were acquired from the near single phase material with nominal composition $UTi_{1.0}Al_{1.0}O_6$ and were analysed by the Rietveld method. The structure of UTi_2O_6 was used as the starting model for structure refine,[36] with the unit cell parameters initially set at the values calculated from a LeBail analysis of X-ray diffraction data (see Section 3.4). The background was fitted using a six term shifted Chebyshev polynomial, followed by systematic

refinement of profile and structure parameters until a satisfactory fit was achieved. Two minor impurity phases were identified in the neutron diffraction pattern, Al_2O_3 (corundum; PDF #04-006-3495; 4.8(1) wt.%) and U_3O_8 (PDF #04-006-7307; 8.9(5) wt.%); the structures of both were included in the refinement.

The refinement rapidly converged to an excellent fit (R_{wp} 4.90%, χ^2 2.041) with 57 variables, 33 of which were structural parameters of the brannerite phase. The final structure parameters and fit are shown in Table 2 and Figure 3 respectively. The Ti / Al ratio was allowed to refine under constraint of full site occupancy and the U site occupancy allowed to refine, affording the composition $UTi_{1.23(1)}Al_{0.77(1)}O_6$ (no change in U site occupancy occurred during refinements). This implies an average U oxidation state of 4.8+, in reasonable agreement with the EDX determined composition of $U_{1.09(6)}Ti_{1.29(3)}Al_{0.71(3)}O_6$, and the X-ray spectroscopy determination of average oxidation state discussed below.

In comparison to the UTi_2O_6 structure reported by Szymanski and Scott[36], the unit cell parameters and overall unit cell volume are smaller, as expected from ionic radii considerations arising from substitution of Al^{3+} (0.675 Å) for Ti^{4+}(0.745 Å), and charge compensation by oxidation of U^{4+} (1.03 Å) to U^{5+} (0.90 Å; ionic radii are for 6-fold co-ordination[37]). The UO_6 octahedra are relatively compact in $UTi_{1.23(1)}Al_{0.77(1)}O_6$, with an average U-O bond length of 2.2034(3) Å, compared to 2.2813 Å in UTi_2O_6, and more distorted relative to a regular octahedron (quadratic elongation, 1.052(1) and bond angle variance 169.4(3) $^{\circ 2}$; compared to 1.047(2) and 156.1(3) $^{\circ 2}$ for UTi_2O_6).

The BO_6 octahedra in $UTi_{1.23(1)}Al_{0.77(1)}O_6$ also displayed a similar compaction and increase in distortion compared to the TiO_6 octahedra in UTi_2O_6. The average (Ti,Al)-O bond distance in

$UTi_{1.23(1)}Al_{0.77(1)}O_6$ was 1.9406(3) Å (compared to 1.9625 Å in UTi_2O_6), with a quadratic elongation of 1.037(1) and bond angle variance of 116.4(3) °^{2} (1.035(2) and 110.6(3) °^{2} respectively for UTi_2O_6). These structural changes are linked to the decreases in ionic radii of both U (on partial oxidation from U^{4+} to U^{5+}) and B (as Ti^{4+} is partially substituted by Al^{3+}).

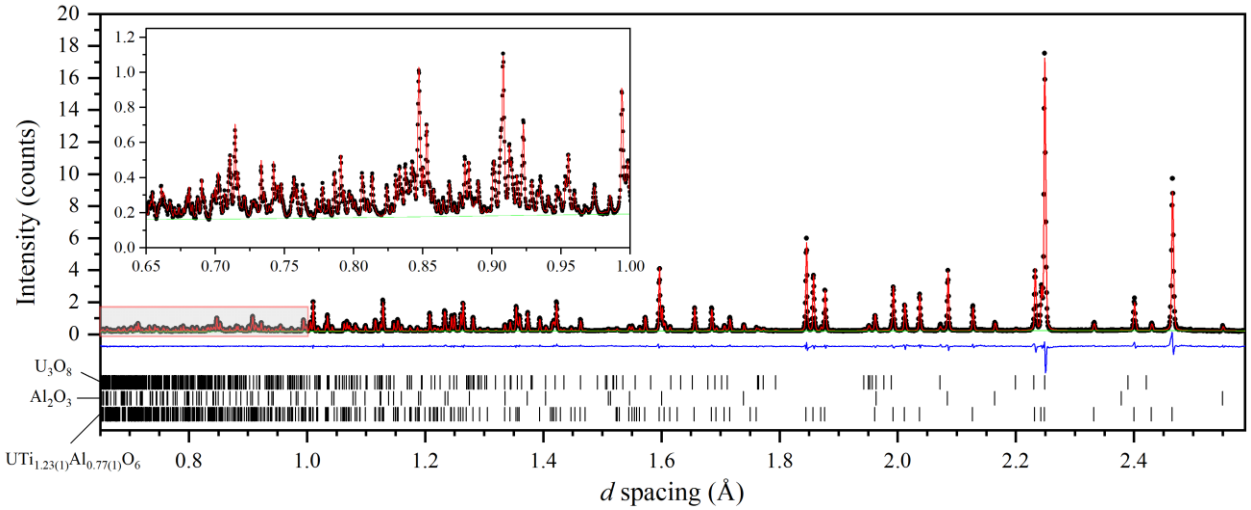

Figure 3: Rietveld refinement fit (y_{calc}; red line) of the neutron time-of-flight diffraction pattern (y_{obs}; black circles) of a material with as-refined composition $U_{1.00(1)}Ti_{1.23(1)}Al_{0.77(1)}O_6$. The allowed reflections for the three phases present ($UTi_{1.23(1)}Al_{0.77(1)}O_6$, U_3O_8, Al_2O_3) are shown as black tick marks.

Table 2: Structural parameters of a material with as-refined composition $UTi_{1.23(1)}Al_{0.77(1)}O_6$, as determined from time-of-flight neutron powder diffraction data.

C2/m (12)		*a*: 9.68255(3) Å	*b*: 3.68910(1) Å	*c*: 6.69628(2) Å	β: 118.548(1)°		V: 210.108(1) Å^3		
Atom	Site	x	y	z	*f*(occ)	U_{11}	U_{22}	U_{33}	U_{13}
U	2a	0	0	0	1	1.22(5)	0.40(4)	0.97(6)	0.53(5)
Ti	4i	0.8255(9)	0	0.3858(12)	0.614(4)	2.18(5)	1.09(4)	1.23(4)	1.05(3)
Al	4i	0.8255(9)	0	0.3858(12)	0.386(4)	2.18(5)	1.09(4)	1.23(4)	1.05(3)
O	4i	0.9779(1)	0	0.3026(2)	1	0.97(5)	1.08(4)	1.08(6)	0.49(5)
O	4i	0.6487(1)	0	0.1008(2)	1	1.03(5)	1.10(4)	1.11(5)	0.32(4)
O	4i	0.2815(1)	0	0.4033(2)	1	1.46(5)	0.42(4)	1.76(5)	1.13(4)
		χ^2: 2.04	R_{wp}: 4.90%	R_p: 4.50%			U_{aniso} × 100 Å^2		

3.3. SEM-EDX

Scanning electron microscopy (SEM) with coupled energy dispersive X-ray spectroscopy (EDX) was primarily used to investigate the compositions of the brannerite phases formed within the multiphase products described above. The microstructures of the produced materials were also examined by backscattered electron imaging.

All samples were porous and poorly sintered, with some pores large enough to have filled with epoxy resin during sample preparation. Compositions that were near single phase brannerite exhibited the lowest porosity, but with evident accessory phases of Ti and Al oxides (*e.g.* the material with nominal composition $UTi_{1.0}Al_{1.0}O_6$, see Figure 4b). Compositions identified as producing grossly multiphase products contained many large pores (*e.g.* the material with nominal composition $UTi_{0.4}Al_{1.6}O_6$, see Figure 4c).

Semi-quantitative energy dispersive X-ray spectroscopy (EDX) was used to examine the Ti:Al ratios of the brannerite phases produced (see Table 1). The Al content of the brannerite phase was found to increase alongside the increase in nominal Al content (*i.e.* as x in $UTi_{2-x}Al_xO_6$ increased from 0.2 to 1.8). The brannerite with the highest Ti content was produced in the material with nominal composition $UTi_{1.8}Al_{0.2}O_6$, and was rich in Al compared to the overall batch stoichiometry, with a determined composition of $U_{0.93(6)}Ti_{1.64(3)}Al_{0.36(3)}O_6$.

The nominal composition $UTi_{1.0}Al_{1.0}O_6$ produced a brannerite phase with determined composition $U_{1.09(6)}Ti_{1.29(3)}Al_{0.71(3)}O_6$. This suggested that some U^{4+} remained after heat treatment, as insufficient Al^{3+} was present to charge-compensate the presence of U^{5+} only. This was in agreement with the average U oxidation state determined by U L_3 ($U^{4.9(1)+}$) and HERFD U M_4 edge

($U^{4.77(2)+}$) XANES, and the evident U^{4+} contribution to the HERFD U M_4 XANES, as discussed below.

The brannerites produced in nominal compositions with the highest Al incorporations, $UTi_{0.4}Al_{1.6}O_6$ and $UTi_{0.2}Al_{1.8}O_6$, had, within error, the same determined compositions $U_{0.91(6)}Ti_{1.01(3)}Al_{0.99(3)}O_6$ and $U_{0.89(6)}Ti_{1.00(3)}Al_{1.00(3)}O_6$ respectively. Following the expected charge compensation of $U^{4+} + Ti^{4+}$ for $U^{5+} + Al^{3+}$, this suggested that all U in these brannerite phases was present as U^{5+}, charge-balanced by 1 f.u. of Al^{3+}. As both compositions produced brannerites of the same stoichiometry, the limit of Al solid solubility in the air-fired system $UTi_{2-x}Al_xO_6$ is at x = 1, where half of the Ti^{4+} is substituted for Al^{3+}.

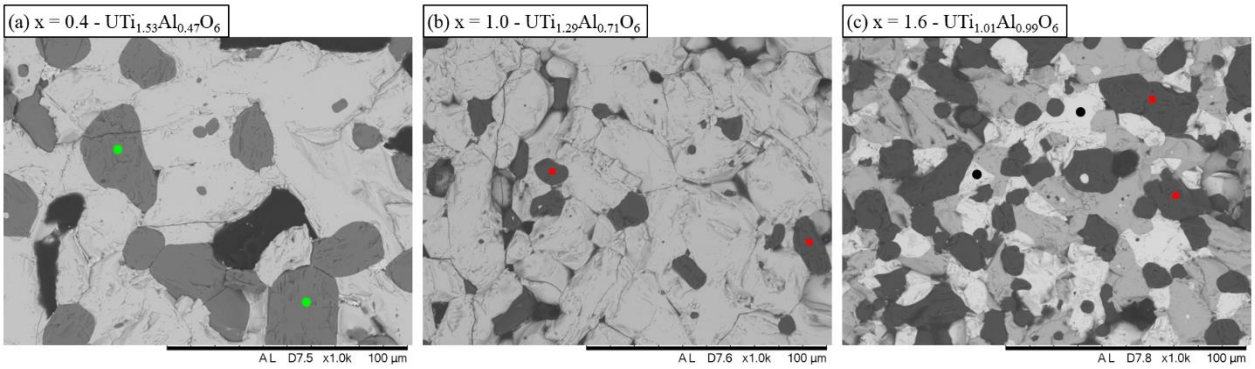

Figure 4: Representative SEM micrographs of materials with nominal compositions in the system $UTi_{2-x}Al_xO_6$: (a) x = 0.4; (b) x = 1.0; and (c) x = 1.6. Brannerite is present in all micrographs as the brightest phase in (a, b); and second brightest in (c). Some regions of the other phases present are marked with: black circle, U_3O_8 (c, white); green circle, TiO_2 (a, dark grey); red square, Al_2O_3 (b, c, dark grey). The darkest regions of each micrograph are pores.

3.4. U L_3 and HERFD M_4 edge XANES

The charge compensation mechanism in the $UTi_{2-x}Al_xO_6$ solid solution was investigated by X-ray absorption spectroscopy at the U L_3 and HERFD M_4 edges. Initially, conventional U L_3 edge XANES were acquired in transmission mode, from all compositions using a laboratory X-ray spectrometer, providing a convenient survey of the average U oxidation state. These data were

utilised to guide acquisition of high resolution fluorescence detected (HERFD) U M_4-edge XANES from selected compositions of particular interest, to determine the specific contributions of U^{4+}, U^{5+} and U^{6+} to average U oxidation state (Ref. Kvashnina et al. PRL, 2013, doi: 10.1103/PhysRevLett.111.253002).

In U L_3 edge XANES, the energy position of the absorption edge is correlated with the oxidation state of the U absorber species. In this work, the position in energy of the edge, E_0, was taken as the energy at half the edge step. The L_3-edge spectra of two well-characterised brannerite-structured reference compounds, $U^{4+}Ti_2O_6$ and $U^{5+}_{0.5}Yb_{0.5}Ti_2O_6$, were also measured, with E_0 values of 17157.02 eV and 17158.53 eV respectively. The spectra of the $UTi_{2-x}Al_xO_6$ compositions examined here had E_0 values close to that of the U^{5+} brannerite reference (see Figure 5a), suggesting the majority of U was present as U^{5+}. Linear interpolation of the measured E_0 values with respect to U oxidation state was performed, with all compositions having average U oxidation states of 4.7+ or higher (see Table 3).

Further analysis of the U L_3 edge spectra was limited by both the instrumental resolution and the multiphase nature of some compositions. For example, composition $UTi_{0.2}Al_{1.8}O_6$ contained a significant fraction of U in U_3O_8 (average U oxidation state of $5.3\dot{3}$). To further elucidate the trend in U oxidation state in these materials, HERFD (high energy resolution fluorescence detected) U M_4 edge XANES were acquired on selected $UTi_{2-x}Al_xO_6$ compositions containing no (x = 0.6, 1.0) or little (x = 1.2) U_3O_8.

Examination of the HERFD M_4 edge spectra (see Figure 5b) showed that the majority of U in all compositions was present as U^{5+}, with a smaller fraction of U^{4+}, in excellent agreement with the laboratory U L_3 edge XANES. Linear combination fitting (LCF) of the spectra was undertaken to

obtain a better qualitative description of the average U oxidation state, utilising the spectra of UTi_2O_6, $CrUO_4$, and $CaUO_4$ as reference compounds of known oxidation state. The best fits obtained for each spectrum are shown in Figure 5c, d, and e (the refined fraction of $CaUO_4$ in each fit was zero). The contribution of UTi_2O_6 to the fit was highest for the nominal composition $UTi_{1.4}Al_{0.6}O_6$ (determined composition $U_{1.05(6)}Ti_{1.46(3)}Al_{0.54(3)}O_6$), suggesting this material had the lowest average U oxidation state. Similarly, the best fit of the spectrum of composition $UTi_{0.8}Al_{1.2}O_6$ (determined composition $U_{1.00(6)}Ti_{1.27(3)}Al_{0.73(3)}O_6$) had smallest contribution from UTi_2O_6, suggesting this material had the highest average U oxidation state. The fit of the spectrum of composition $UTi_{1.0}Al_{1.0}O_6$ (determined composition $U_{1.09(6)}Ti_{1.29(3)}Al_{0.71(3)}O_6$) had a contribution from UTi_2O_6 approximately halfway between those of (nominal composition) $UTi_{1.4}Al_{0.6}O_6$ and $UTi_{0.8}Al_{1.2}O_6$.

The overall trends observed in the spectra of both U HERFD M_4 and L_3 edge XANES suggest that the U oxidation state in these materials is primarily controlled by the concentration of Al^{3+} substitution on the Ti^{4+} site. This is in agreement with observations of previously reported mixed U site substituted brannerites.[15,19,21] There was no evidence to support the presence of significant U^{6+} in the U HERFD M_4 edge XANES.

Table 3: Tabulated data extracted from U L_3 and HERFD M_4 edge X-ray absorption spectra of materials with nominal compositions in the system $UTi_{2-x}Al_xO_6$. E_0 was defined as the energy position at half the edge step of the L_3-edge spectra; mean oxidation states were calculated from a linear regression of the three materials of known valence: UTi_2O_6, $U_{0.5}Yb_{0.5}Ti_2O_6$, and the material with nominal composition UAl_2O_6 containing U_3O_8 as the only U-bearing phase.

Nominal x in $UTi_{2-x}Al_xO_6$	Brannerite composition (EDX)	E_0 of L_3 edge (eV)	L_3 edge mean U ox. state	LCF *f*(UTi_2O_6)	LCF *f*($CrUO_4$)	M_4 edge mean U ox. state
0.2	$U_{0.93(6)}Ti_{1.64(3)}Al_{0.36(3)}O_6$	17158.64	5.0(1)	-	-	-
0.4	$U_{1.04(6)}Ti_{1.53(3)}Al_{0.47(3)}O_6$	17158.60	5.0(1)	-	-	-
0.6	$U_{1.05(6)}Ti_{1.46(3)}Al_{0.54(3)}O_6$	17158.55	4.9(1)	0.901	0.303	4.75(2)
0.8	$U_{1.06(6)}Ti_{1.40(3)}Al_{0.60(3)}O_6$	17158.56	4.9(1)	-	-	-
1.0	$U_{1.09(6)}Ti_{1.29(3)}Al_{0.71(3)}O_6$	17158.37	4.8(1)	0.917	0.281	4.77(2)
1.2	$U_{1.00(6)}Ti_{1.27(3)}Al_{0.73(3)}O_6$	17158.11	4.7(1)	0.934	0.243	4.79(2)
1.4	$U_{0.98(6)}Ti_{1.22(3)}Al_{0.78(3)}O_6$	17158.34	4.8(1)	-	-	-
1.6	$U_{0.91(6)}Ti_{1.01(3)}Al_{0.99(3)}O_6$	17158.63	5.0(1)	-	-	-
1.8	$U_{0.89(6)}Ti_{1.00(3)}Al_{1.00(3)}O_6$	17158.94	5.2(1)	-	-	-
2.0	(U_3O_8 formed)	17159.33	$\underline{5.3\dot{3}}$	-	-	-
-	UTi_2O_6	17157.02	$\underline{4}$	-	-	-
-	$U_{0.5}Yb_{0.5}Ti_2O_6$	17158.53	$\underline{5}$	-	-	-

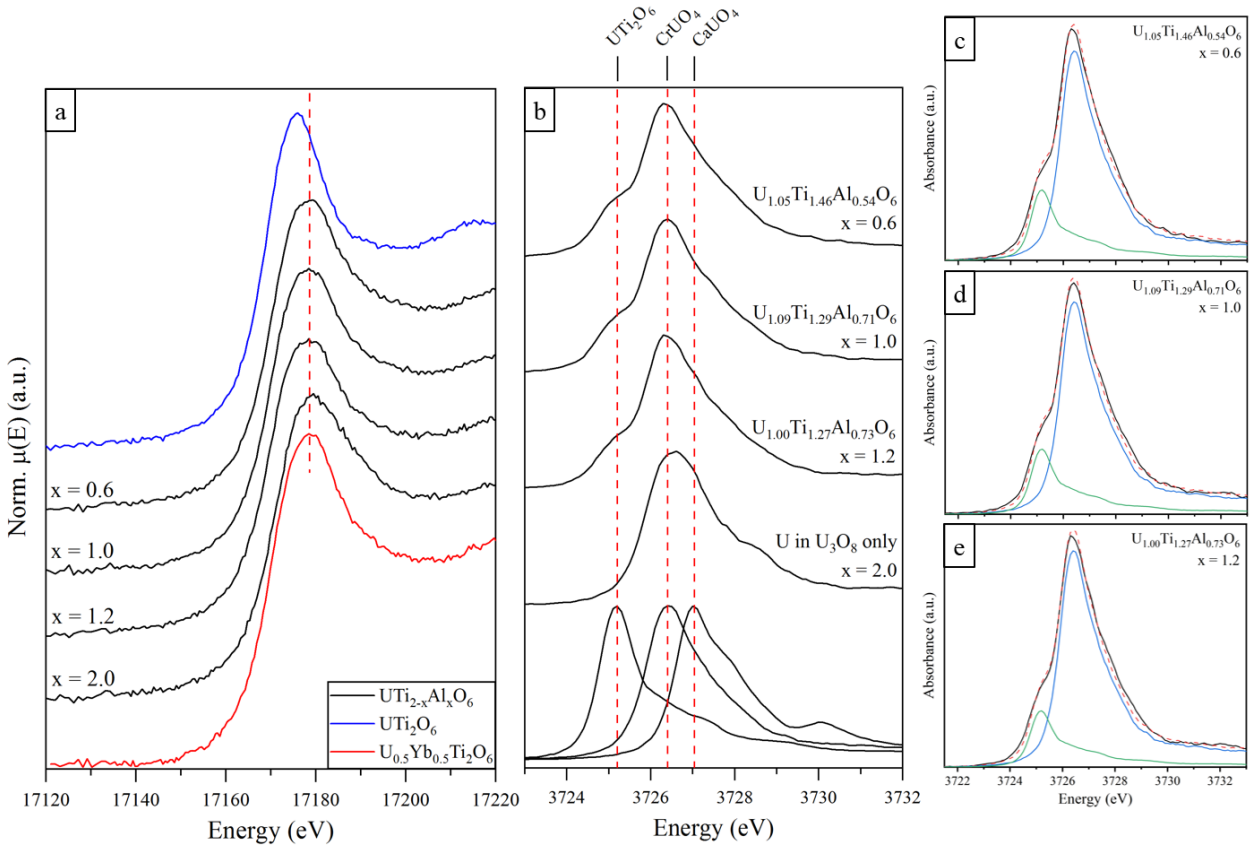

Figure 5: XANES spectra of materials with nominal compositions in the system $UTi_{2-x}Al_xO_6$. (a) Overlaid U L_3 edge XANES spectra of $UTi_{2-x}Al_xO_6$ (x is 0.6, 1.0, 1.2, 2), with UTi_2O_6 and $U_{0.5}Yb_{0.5}Ti_2O_6$ reference compounds (for U^{4+} and U^{5+} respectively). (b) Stacked U HERFD M_4 edge XANES spectra of select compositions, with UTi_2O_6, $CrUO_4$, and $CaUO_4$ reference compounds (for U^{4+}, U^{5+}, and U^{6+} respectively). (c, d, e) linear combination fits (red dashed lines) of $UTi_{2-x}Al_xO_6$ compositions with x = 0.6, 1.0, 1.2, with compositions determined from EDX measurements inset.

3.5. Changes in brannerite phase crystal chemistry

The unit cell parameters of the brannerite compositions were determined using LeBail method refinements of powder XRD patterns. Compositional information was derived from semi-quantitative EDX measurements to aid in determining the actual stoichiometry of the brannerite phases formed. For the purpose of quantifying the trends observed and allowing for comparison between compositions, an average cation radius was calculated, with the assumption that each formula unit of Al^{3+} charge-balanced the equivalent amount of U^{5+}.

As the average ionic radius decreased with increasing Al^{3+} (6-coordinate crystal radius of Al^{3+}, 0.675 Å and Ti^{4+}, 0.745 Å[37]) and U^{5+} contents (6-coordinate crystal radii of U^{4+}, 1.03 Å and U^{5+}, 0.9 Å[37]), the *b* and *c* unit cell parameters and the overall unit cell volume decreased near linearly (δ/max of 0.62%, 0.94% and 1.80% respectively). The *a* unit cell parameter also decreased, but the observed trend was not directly correlated with the decrease in average ionic radius and was of a lower relative magnitude (δ/max of 0.40% in the brannerites reported here). This is in good agreement with previous reports of the trends observed in U-site doped brannerites, where cation size does not have a strongly correlated effect on the *a* parameter.[17,18] The observed angle β exhibited a small and linear increase as the average ionic radius decreased; this corresponds to a decrease in overall unit cell volume.

The brannerite structure, AB_2O_6, is formed of corrugated sheets of edge-sharing (BO_6) distorted octahedra connected by chains of (AO_6) octahedra parallel to the *b*-axis. The geometry of the (BO_6) sheets is complex, but can be described as two-wide 'zig-zag' chains of edge-sharing (BO_6) octahedra parallel to the *b*-axis connected by edge-sharing with neighbouring (BO_6) chains, with the ensemble overall parallel to the *a*-axis (similar arrangements of octahedra are observed in the TiO_2-anatase structure). See Figure 6 for a representation of the structure.

On consideration of the crystal structure, it is apparent that the decrease in average cation size caused by the substitution of Ti^{4+} with Al^{3+} (and the associated change in average U oxidation state) has differing impacts on the three unit cell lengths. The strong correlation with the *b* parameter appears to be primarily caused by the edge-sharing (AO_6) chains directly parallel to *b*, with the 'zig-zag' (BO_6) chains having an additional, but lesser contribution. Changes in the *c* parameter are primarily controlled by the (AO_6) octahedra, as the O1-A-O1 bonds are parallel to the *c*-axis,

with changes in bond length causing corresponding changes in the spacing of the (BO_6) sheets. The lack of strong correlation between average cationic radius and the *a* parameter is likely due to the tilting of the 'zig-zag' (BO_6) chains relative to the *a* axis: these rigid chains are parallel to *b*, but, though the overall sheets are parallel to *a*, the individual chains are out of plane. This suggests, in agreement with the trends observed here and in the literature, that the changes in the *a* parameter are the result of subtle structural changes.

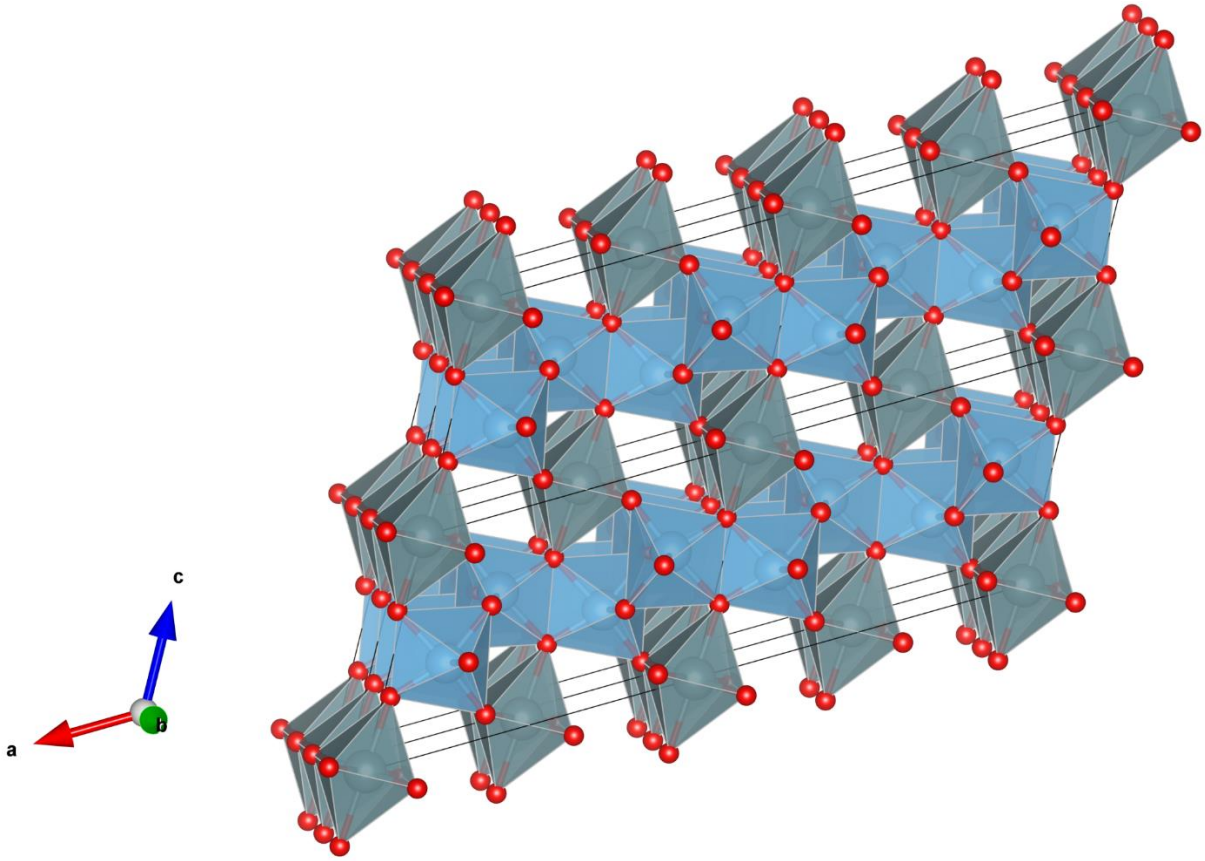

Figure 6: A polyhedral representation of the UTi_2O_6 brannerite structure, as reported by Szymanski and Scott[36], with (AO_6) octahedra in grey, (BO_6) octahedra in light blue, and O atoms in red. The diagram shows a 2×2×2 unit cell ensemble. Produced in the VESTA software package[38].

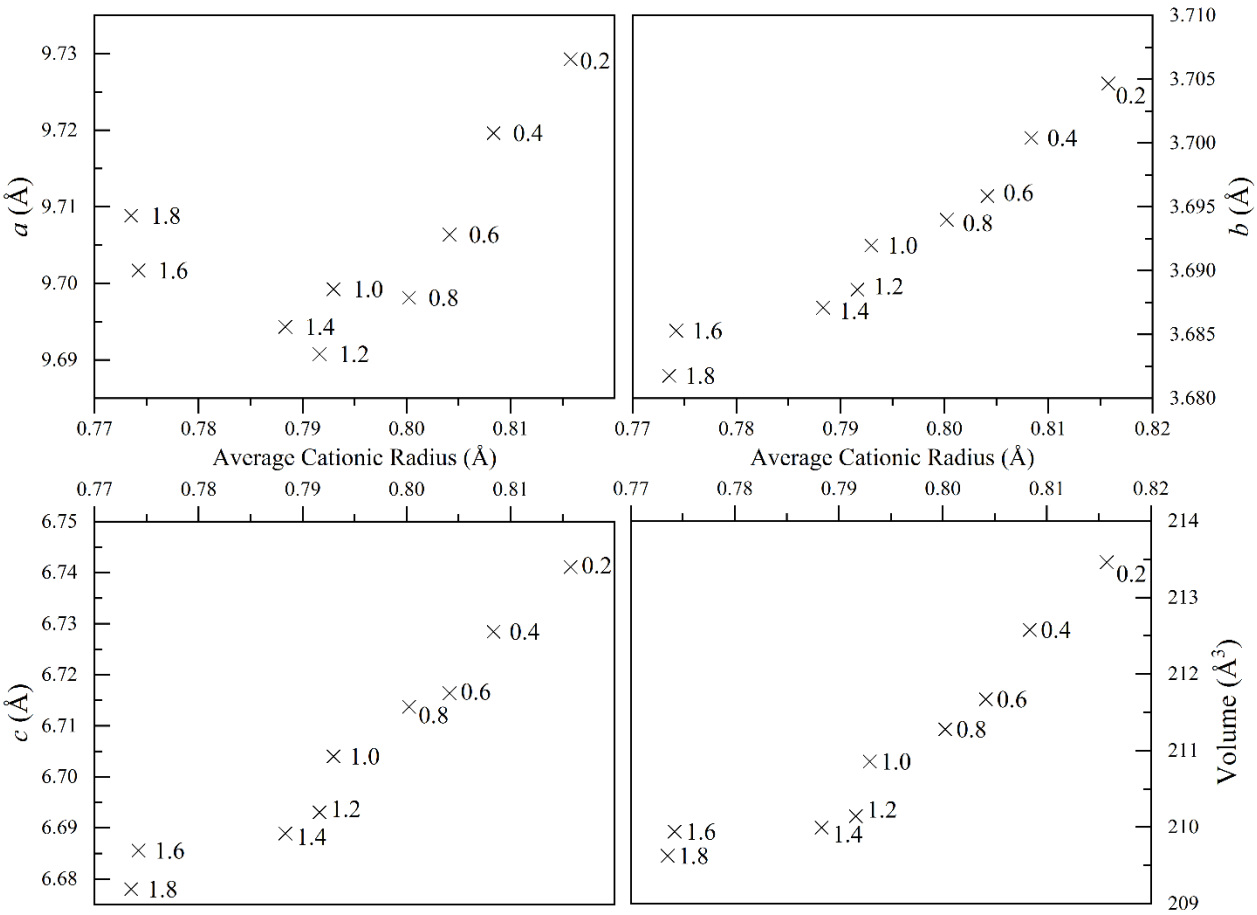

Figure 7: Plots of *a*, *b*, and *c* unit cell parameters and overall unit cell volumes for the brannerite structured phases present in materials with nominal compositions of $UTi_2Al_xO_6$ with $0.2 \leq x \leq 1.8$ (labelled). The overall average cationic radius for each brannerite was calculated as a weighted average of the cation radii, with relative cationic abundances from EDX measurements (U^{5+} content presumed equal to Al^{3+} content).

Table 4: Unit cell parameters and EDX derived approximate compositions for the brannerite structured phases present in materials with nominal compositions $UTi_{2-x}Al_xO_6$. Unit cell parameters were calculated using LeBail method refinements of XRD patterns. The unit cell parameters of $U^{4+}Ti_2O_6$, as previously reported in the literature[36], are included for comparison.

Nominal x in $UTi_{2-x}Al_xO_6$	Brannerite composition	*a* (Å)	*b* (Å)	*c* (Å)	β (°)	Volume (Å^3)	R_{wp}	χ^2
0.2	$U_{0.93(6)}Ti_{1.64(3)}Al_{0.36(3)}O_6$	9.7293(3)	3.7047(1)	6.7411(2)	118.53(1)	213.46(2)	7.10	1.426
0.4	$U_{1.04(6)}Ti_{1.53(3)}Al_{0.47(3)}O_6$	9.7196(2)	3.7004(1)	6.7284(2)	118.55(1)	212.58(1)	7.62	1.509
0.6	$U_{1.05(6)}Ti_{1.46(3)}Al_{0.54(3)}O_6$	9.7064(2)	3.6958(1)	6.7164(2)	118.54(1)	211.67(1)	8.12	1.667
0.8	$U_{1.06(6)}Ti_{1.40(3)}Al_{0.60(3)}O_6$	9.6981(3)	3.6940(1)	6.7137(2)	118.55(1)	211.28(1)	9.75	2.141
1.0	$U_{1.09(6)}Ti_{1.29(3)}Al_{0.71(3)}O_6$	9.6993(2)	3.6920(1)	6.7040(1)	118.56(1)	210.86(1)	7.85	1.621
1.2	$U_{1.00(6)}Ti_{1.27(3)}Al_{0.73(3)}O_6$	9.6908(2)	3.6885(1)	6.6931(1)	118.55(1)	210.15(1)	6.79	1.587
1.4	$U_{0.98(6)}Ti_{1.22(3)}Al_{0.78(3)}O_6$	9.6943(2)	3.6871(1)	6.6889(1)	118.56(1)	210.00(1)	8.08	1.820
1.6	$U_{0.91(6)}Ti_{1.01(3)}Al_{0.99(3)}O_6$	9.7017(2)	3.6853(1)	6.6856(2)	118.56(1)	209.94(1)	7.90	1.858
1.8	$U_{0.89(6)}Ti_{1.00(3)}Al_{1.00(3)}O_6$	9.7088(5)	3.6818(2)	6.6780(3)	118.58(1)	209.63(2)	8.96	2.073
-	UTi_2O_6[36]	9.8123	3.7697	6.9253	118.96	224.14	-	-

4. Discussion

In agreement with the previously reported solid solubility of Fe in air-fired brannerites[23], Al^{3+} is highly soluble in the brannerite structure. From the phase assemblages produced in this work it is apparent that, whilst the solubility the Al^{3+} is closely related to the average U oxidation state, when synthesised in an air atmosphere the structure is chemically flexible, supporting varied Al^{3+} content and mixed $U^{4/5+}$ oxidation state. Initially it was expected that the addition of greater than 1 f.u. of Al^{3+} would allow for charge compensation of a fraction of U^{6+}, supported by both sufficient charge-balancing species and the decrease in unit cell size; however, there was no evidence of brannerite U oxidation states greater than 5+ from either the U L_3 or HERFD M_4-edge XANES, and no evidence of any U6+ contribution to HERFD M_4-edge XANES.

The use of an aliovalent Ti-site dopant has allowed for close examination of changes in the crystal chemistry of the brannerite structure. The observed changes in the unit cell parameters are similar

to those reported for U-site doping, with *b*, *c*, and the overall unit cell volume being strongly correlated to the average cationic radius, with the *a* parameter having a secondary response only. Due to ionic size considerations, it is expected that Al^{3+} was present on the Ti^{4+} site only, though further characterisation of the cationic coordination environments is necessary. The addition of up to 1 f.u. of Al^{3+} and U^{5+} into the brannerite structure results in an increase in relative B-site cationic radius, as evidenced by an increase in the ratio r(B)/r(A) from 0.723 in stoichiometric UTi_2O_6, to 0.789 in the sample with nominal composition $UTi_{0.2}Al_{1.8}O_6$ (brannerite composition approx. $U_{0.89(6)}Ti_{1.00(3)}Al_{1.00(3)}O_6$).

5. Conclusions

This investigation has synthesised and characterised a novel U^{5+} brannerite with composition $U_{1.00(1)}Ti_{1.23(1)}Al_{0.77(1)}O_6$. The structure of this material was examined using TOF powder neutron diffraction, with Al^{3+} substitution on the Ti-site leading to shrinkage of the unit cell and increased distortion of the UO_6 and $(Ti,Al)O_6$ octahedra compared to UTi_2O_6.

The compositional system $UTi_{2-x}Al_xO_6$ was synthesised at 1400 °C under an air atmosphere, producing multiphase samples containing Al-doped brannerites as the major phase. The crystal chemistry of the brannerite phases produced has been examined, utilising LeBail method refinements of XRD data and U L_3 and HERFD M_4 edge XANES. The trends observed are in excellent agreement with those previously observed in U-site doped brannerites, with cationic sizes having a strong, linear effect on the *b* and *c* unit cell parameters, as well as the overall unit cell volume.

The brannerites produced display a relatively wide compositional range, with EDX-derived compositions from $U_{0.93(6)}Ti_{1.64(3)}Al_{0.36(3)}O_6$ to $U_{0.89(6)}Ti_{1.00(3)}Al_{1.00(3)}O_6$, demonstrating an

unexpected degree of chemical flexibility with respect to Al^{3+} content and U oxidation state, despite the oxidising process atmosphere. The average U oxidation state in the brannerite phases increased towards U^{5+} as the relative amount of Al^{3+} increased.

The use of a high fraction, lower valence Ti-site dopant to charge balance U^{5+} has been successfully demonstrated, with additions of Al^{3+} stabilising the brannerite structure when fired in air, whilst allowing for retention of the full U content. The limit of solid solubility of Al^{3+} in the air-fired system $UTi_{2-x}Al_xO_6$ has been inferred to be when x = 1. No evidence for the possibility of Al content higher than 1 f.u., charge-balancing U^{6+}, in the brannerite structure was found.

6. Acknowledgments

This research utilised the HADES/MIDAS[39] facility at the University of Sheffield established with financial support from EPSRC and BEIS, under grant EP/T011424/1. The experiment at HRPD, ISIS Neutron and Muon Source was supported by beamtime allocation RB2000257[29]; and the authors would like to thank Dr. A. D. Fortes for assistance with data acquisition. MDW is grateful to the UK EPSRC and Nuclear Decommissioning Authority for providing studentship through an EPSRC iCASE award. Needs CLC Fellowship, ESRF (for the beamtime allocation at BM20 beamline). We acknowledge a help from Tatiana Polyakova, Anastasiia Smirnova, Jurij Galanzew from BM20 Beamline of ESRF during the U M4 HERFD data collection. K.O.K. acknowledges the support from the European Research Council (ERC) under grant no. 759696.

References

(1) Charalambous, F. A.; Ram, R.; Pownceby, M. I.; Tardio, J.; Bhargava, S. K. Chemical and Microstructural Characterisation Studies on Natural and Heat Treated Brannerite Samples.

Miner. Eng. **2012**, *39* (Supplement C), 276–288. https://doi.org/10.1016/j.mineng.2012.08.006.

(2) Turuani, M.; Choulet, F.; Eglinger, A.; Goncalves, P.; Machault, J.; Mercadier, J.; Seydoux-Guillaume, A.-M.; Reynaud, S.; Baron, F.; Beaufort, D.; Batonneau, Y.; Gouy, S.; Mesbah, A.; Szenknect, S.; Dacheux, N.; Chapon, V.; Pagel, M. Geochemical Fingerprints of Brannerite (UTi2O6): An Integrated Study. *Mineral. Mag.* **2020**, *84* (2), 313–334. https://doi.org/10.1180/mgm.2020.7.

(3) Lumpkin, G. R.; Leung, S. H. F.; Ferenczy, J. Chemistry, Microstructure, and Alpha Decay Damage of Natural Brannerite. *Chem. Geol.* **2012**, *291*, 55–68. https://doi.org/10.1016/j.chemgeo.2011.09.008.

(4) Lian, J.; Wang, L. M.; Lumpkin, G. R.; Ewing, R. C. Heavy Ion Irradiation Effects of Brannerite-Type Ceramics. *Nucl. Instrum. Methods Phys. Res. Sect. B Beam Interact. Mater. At.* **2002**, *191* (1), 565–570. https://doi.org/10.1016/S0168-583X(02)00611-0.

(5) Lumpkin, G. R.; Smith, K. L.; Blackford, M. G. Heavy Ion Irradiation Studies of Columbite, Brannerite, and Pyrochlore Structure Types. *J. Nucl. Mater.* **2001**, *289* (1), 177–187. https://doi.org/10.1016/S0022-3115(00)00695-4.

(6) Lin, H.; Szenknect, S.; Mesbah, A.; Baron, F.; Beaufort, D.; Batonneau, Y.; Mercadier, J.; Eglinger, A.; Turuani, M.; Seydoux-Guillaume, A.-M.; Goncalves, P.; Choulet, F.; Chapon, V.; Pagel, M.; Dacheux, N. A Multiparametric Study on the Dissolution of Synthetic Brannerite. *Npj Mater. Degrad.* **2021**, *5* (1), 1–9. https://doi.org/10.1038/s41529-021-00173-6.

(7) Charalambous, F. A.; Ram, R.; McMaster, S.; Tardio, J.; Bhargava, S. K. An Investigation on the Dissolution of Synthetic Brannerite (UTi2O6). *Hydrometallurgy* **2013**, *139* (Supplement C), 1–8. https://doi.org/10.1016/j.hydromet.2013.06.017.

(8) Vance, E. R.; Watson, J. N.; Carter, M. L.; Day, R. A.; Begg, B. D. Crystal Chemistry and Stabilization in Air of Brannerite, UTi2O6. *J. Am. Ceram. Soc.* **2001**, *84* (1), 141–144. https://doi.org/10.1111/j.1151-2916.2001.tb00621.x.

(9) Kaiman, S. Synthesis of Brannerite. *Can. Mineral.* **1959**, *6* (3), 389–390.

(10) Patchett, J. E.; Nuffield, E. W. Studies of Radioactive Compounds. X. The Synthesis and Crystallography of Brannerite. *Can. Mineral.* **1960**, *6* (4), 483–490.

(11) Mesbah, A.; Szenknect, S.; Clavier, N.; Lin, H.; Baron, F.; Beaufort, D.; Batonneau, Y.; Mercadier, J.; Eglinger, A.; Turuani, M.; Goncalves, P.; Choulet, F.; Chapon, V.; Seydoux-Guillaume, A.-M.; Pagel, M.; Dacheux, N. Direct Synthesis of Pure Brannerite UTi2O6. *J. Nucl. Mater.* **2019**, *515*, 401–406. https://doi.org/10.1016/j.jnucmat.2019.01.003.

(12) Bailey, D. J.; Stennett, M. C.; Hyatt, N. C. Synthesis and Characterization of Brannerite Wasteforms for the Immobilization of Mixed Oxide Fuel Residues. *Procedia Chem.* **2016**, *21*, 371–377. https://doi.org/10.1016/j.proche.2016.10.052.

(13) James, M.; Carter, M. L.; Watson, J. N. The Synthesis, Crystal Chemistry and Structures of Y-Doped Brannerite (U1−xYxTi2O6) and Thorutite (Th1−xYxTi2O6−δ) Phases. *J. Solid State Chem.* **2003**, *174* (2), 329–333. https://doi.org/10.1016/S0022-4596(03)00230-5.

(14) Stefanovsky, S. V.; Yudintsev, S. V.; Shiryaev, A. A.; Murzin, V. Y.; Trigub, A. L. Phase Partitioning and Uranium Speciation in Brannerite-Based Ceramics. *J. Eur. Ceram. Soc.* **2017**, *37* (2), 771–777. https://doi.org/10.1016/j.jeurceramsoc.2016.08.028.

(15) Zhang, Y.; Karatchevtseva, I.; Kong, L.; Wei, T.; Zhang, Z. Structural and Spectroscopic Investigations on the Crystallization of Uranium Brannerite Phases in Glass. *J. Am. Ceram. Soc.* **2018**, *101* (11), 5219–5228. https://doi.org/10.1111/jace.15750.

(16) Zhang, Y.; Kong, L.; Aughterson, R. D.; Karatchevtseva, I.; Zheng, R. Phase Evolution from Ln2Ti2O7 (Ln=Y and Gd) Pyrochlores to Brannerites in Glass with Uranium Incorporation. *J. Am. Ceram. Soc.* **2017**, *100* (11), 5335–5346. https://doi.org/10.1111/jace.15051.

(17) Zhang, Y.; Kong, L.; Karatchevtseva, I.; Aughterson, R. D.; Gregg, D. J.; Triani, G. Development of Brannerite Glass-Ceramics for the Immobilization of Actinide-Rich Radioactive Wastes. *J. Am. Ceram. Soc.* **2017**, *100* (9), 4341–4351. https://doi.org/10.1111/jace.14975.

(18) Zhang, Y.; Wei, T.; Zhang, Z.; Kong, L.; Dayal, P.; Gregg, D. J. Uranium Brannerite with Tb(III)/Dy(III) Ions: Phase Formation, Structures, and Crystallizations in Glass. *J. Am. Ceram. Soc.* **2019**, *102* (12), 7699–7709. https://doi.org/10.1111/jace.16657.

(19) Dixon Wilkins, M. C.; Stennett, M. C.; Hyatt, N. C. The Effect of A-Site Cation on the Formation of Brannerite (ATi2O6, A = U, Th, Ce) Ceramic Phases in a Glass-Ceramic Composite System. *MRS Adv.* **2020**, *5* (1–2), 73–81. https://doi.org/10.1557/adv.2019.470.

(20) James, M.; Watson, J. N. The Synthesis and Crystal Structure of Doped Uranium Brannerite Phases U1−xMxTi2O6 (M=Ca2+, La3+, and Gd3+). *J. Solid State Chem.* **2002**, *165* (2), 261–265. https://doi.org/10.1006/jssc.2002.9519.

(21) Bailey, D. J.; Stennett, M. C.; Ravel, B.; Grolimund, D.; Hyatt, N. C. Synthesis and Characterisation of Brannerite Compositions (U0.9Ce0.1)1−xMxTi2O6 (M = Gd3+, Ca2+) for the Immobilisation of MOX Residues. *RSC Adv.* **2018**, *8* (4), 2092–2099. https://doi.org/10.1039/C7RA11742F.

(22) Bailey, D. J.; Stennett, M. C.; Hyatt, N. C. Synthesis and Characterization of Brannerite Compositions for MOX Residue Disposal. *MRS Adv.* **2017**, *2* (10), 557–562. https://doi.org/10.1557/adv.2016.631.

(23) Vance, E. R.; Watson, J. N.; Carter, M. L.; Day, R. Crystal Chemistry, Radiation Effects and Aqueous Leaching of Brannerite, UTi2O6. *Ceram. Trans.* **1999**, *107*, 561–568.

(24) Vance, E. R.; Carter, M. L.; Lumpkin, G. R.; Day, R. A.; Begg, B. D. *Solid Solubilities of Pu, U, Gd and Hf in Candidate Ceramic Nuclear Wasteforms*; DOE/ER/45676, Project Number 60387, 781161; 2001. https://doi.org/10.2172/781161.

(25) Vance, E. R.; Carter, M. L.; Stewart, M. W. A.; Day, R. A.; Begg, B. D.; Ball, C. J. Ionic Size Limits for A Ions in Brannerite (ATi2O6) and Pyrochlore (CaATi2O7) Titanate Structures (A = Tetravalent Rare Earths and Actinides). *MRS Online Proc. Libr. Arch.* **2002**, *713*. https://doi.org/10.1557/PROC-713-JJ2.6.

(26) Gates-Rector, S.; Blanton, T. The Powder Diffraction File: A Quality Materials Characterization Database. *Powder Diffr.* **2019**, *34* (4), 352–360. https://doi.org/10.1017/S0885715619000812.

(27) Coelho, A. A. TOPAS and TOPAS-Academic: An Optimization Program Integrating Computer Algebra and Crystallographic Objects Written in C++. *J. Appl. Crystallogr.* **2018**, *51* (1), 210–218. https://doi.org/10.1107/S1600576718000183.

(28) Evans, J. Advanced Input Files & Parametric Quantitative Analysis Using Topas. *Mater. Sci. Forum* **2010**, *651*, 1–9. https://doi.org/10.4028/www.scientific.net/MSF.651.1.

(29) Hyatt, N. C. Investigation into the Structural Relations of Actinide Brannerites. *STFC ISIS Neutron Muon Source* **2021**. https://doi.org/10.5286/ISIS.E.RB2000257.

(30) Arnold, O.; Bilheux, J. C.; Borreguero, J. M.; Buts, A.; Campbell, S. I.; Chapon, L.; Doucet, M.; Draper, N.; Ferraz Leal, R.; Gigg, M. A.; Lynch, V. E.; Markvardsen, A.; Mikkelson, D. J.; Mikkelson, R. L.; Miller, R.; Palmen, K.; Parker, P.; Passos, G.; Perring, T. G.; Peterson, P. F.; Ren, S.; Reuter, M. A.; Savici, A. T.; Taylor, J. W.; Taylor, R. J.; Tolchenov, R.; Zhou, W.; Zikovsky, J. Mantid—Data Analysis and Visualization Package for Neutron Scattering and μ SR Experiments. *Nucl. Instrum. Methods Phys. Res. Sect. Accel. Spectrometers Detect. Assoc. Equip.* **2014**, *764*, 156–166. https://doi.org/10.1016/j.nima.2014.07.029.

(31) Seidler, G. T.; Mortensen, D. R.; Remesnik, A. J.; Pacold, J. I.; Ball, N. A.; Barry, N.; Styczinski, M.; Hoidn, O. R. A Laboratory-Based Hard x-Ray Monochromator for High-Resolution x-Ray Emission Spectroscopy and x-Ray Absorption near Edge Structure Measurements. *Rev. Sci. Instrum.* **2014**, *85* (11), 113906. https://doi.org/10.1063/1.4901599.

(32) Jahrman, E. P.; Holden, W. M.; Ditter, A. S.; Mortensen, D. R.; Seidler, G. T.; Fister, T. T.; Kozimor, S. A.; Piper, L. F. J.; Rana, J.; Hyatt, N. C.; Stennett, M. C. An Improved Laboratory-Based x-Ray Absorption Fine Structure and x-Ray Emission Spectrometer for Analytical Applications in Materials Chemistry Research. *Rev. Sci. Instrum.* **2019**, *90* (2), 024106. https://doi.org/10.1063/1.5049383.

(33) Mottram, L. M.; Dixon Wilkins, M. C.; Blackburn, L. R.; Oulton, T.; Stennett, M. C.; Sun, S. K.; Corkhill, C. L.; Hyatt, N. C. A Feasibility Investigation of Laboratory Based X-Ray Absorption Spectroscopy in Support of Nuclear Waste Management. *MRS Adv.* **2020**, *In Print*, 1–9. https://doi.org/10.1557/adv.2020.44.

(34) Ravel, B.; Newville, M. ATHENA and ARTEMIS: Interactive Graphical Data Analysis Using IFEFFIT. *Phys. Scr.* **2005**, *2005* (T115), 1007. https://doi.org/10.1238/Physica.Topical.115a01007.

(35) Ravel, B.; Newville, M. ATHENA, ARTEMIS, HEPHAESTUS: Data Analysis for X-Ray Absorption Spectroscopy Using IFEFFIT. *J. Synchrotron Radiat.* **2005**, *12* (4), 537–541. https://doi.org/10.1107/S0909049505012719.

(36) Szymanski, J. T.; Scott, J. D. A Crystal-Structure Refinement of Synthetic Brannerite, UTi 2 O 6 , and Its Bearing on Rate of Alkaline-Carbonate Leaching of Brannerite in Ore. *Can. Mineral.* **1982**, *20* (2), 271–280.

(37) Shannon, R. D. Revised Effective Ionic Radii and Systematic Studies of Interatomic Distances in Halides and Chalcogenides. *Acta Crystallogr. A* **1976**, *32* (5), 751–767. https://doi.org/10.1107/S0567739476001551.

(38) Momma, K.; Izumi, F. VESTA 3 for Three-Dimensional Visualization of Crystal, Volumetric and Morphology Data. *J. Appl. Crystallogr.* **2011**, *44* (6), 1272–1276. https://doi.org/10.1107/S0021889811038970.

(39) Hyatt, N. C.; Corkhill, C. L.; Stennett, M. C.; Hand, R. J.; Gardner, L. J.; Thorpe, C. L. The HADES Facility for High Activity Decommissioning Engineering & Science: Part of the UK National Nuclear User Facility. *IOP Conf. Ser. Mater. Sci. Eng.* **2020**, *818*, 012022. https://doi.org/10.1088/1757-899X/818/1/012022.